

RESEARCH BRIEF

The Rodent Liver Undergoes Weaning-Induced Involution and Supports Breast Cancer Metastasis

Erica T. Goddard¹, Ryan C. Hill², Travis Nemkov², Angelo D'Alessandro², Kirk C. Hansen², Ori Maller³, Solange Mongoue-Tchokote⁴, Motomi Mori^{4,5}, Ann H. Partridge⁶, Virginia F. Borges^{7,8,9}, and Pepper Schedin^{1,4,9}

ABSTRACT

Patients with postpartum breast cancer are at increased risk for metastasis compared with age-matched nulliparous or pregnant patients. Here, we address whether circulating tumor cells have a metastatic advantage in the postpartum host and find the postlactation rodent liver preferentially supports metastasis. Upon weaning, we observed liver weight loss, hepatocyte apoptosis, extracellular matrix remodeling including deposition of collagen and tenascin-C, and myeloid cell influx, data consistent with weaning-induced liver involution and establishment of a prometastatic microenvironment. Using intracardiac and intraportal metastasis models, we observed increased liver metastasis in post-weaning BALB/c mice compared with nulliparous controls. Human relevance is suggested by a ~3-fold increase in liver metastasis in patients with postpartum breast cancer ($n = 564$) and by liver-specific tropism ($n = 117$). In sum, our data reveal a previously unknown biology of the rodent liver, weaning-induced liver involution, which may provide insight into the increased liver metastasis and poor prognosis of women diagnosed with postpartum breast cancer.

SIGNIFICANCE: We find that patients with postpartum breast cancer are at elevated risk for liver metastasis. We identify a previously unrecognized biology, namely weaning-induced liver involution, that establishes a prometastatic microenvironment, and which may account in part for the poor prognosis of patients with postpartum breast cancer. *Cancer Discov*; 7(2); 1-11. ©2016 AACR.

INTRODUCTION

Breast cancers diagnosed within 5 years of childbirth impart a ~3-fold increased risk for metastasis compared with breast cancers diagnosed in age-matched nulliparous or pregnant

women (1–3). Increased metastasis has been found to be independent of tumor estrogen receptor, progesterone receptor, or HER2 expression, or tumor stage (2), implicating a host biology specific to the postpartum period. In rodents, the postpartum event of weaning-induced mammary gland involution

¹Department of Cell, Developmental and Cancer Biology, Oregon Health & Science University, Portland, Oregon. ²Department of Biochemistry and Molecular Genetics, University of Colorado Denver, Aurora, Colorado. ³Department of Surgery, Center for Bioengineering and Tissue Regeneration, University of California, San Francisco, San Francisco, California. ⁴Knight Cancer Institute, Oregon Health & Science University, Portland, Oregon. ⁵School of Public Health, Oregon Health & Science University, Portland, Oregon. ⁶Department of Medical Oncology, Dana-Farber Cancer Institute, Boston, Massachusetts. ⁷Department of Medicine, Division of Medical Oncology, University of Colorado Anschutz Medical Campus, Aurora, Colorado. ⁸University of Colorado Cancer Center, Aurora, Colorado. ⁹Young Women's Breast Cancer Translational Program, University of Colorado Anschutz Medical Campus, Aurora, Colorado.

Note: Supplementary data for this article are available at Cancer Discovery Online (<http://cancerdiscovery.aacrjournals.org/>).

V.F. Borges and P. Schedin contributed equally to this article.

Corresponding Authors: Pepper Schedin, Oregon Health & Science University, 3181 SW Sam Jackson Park Road, Portland, OR 97239. Phone: 503-494-3565; Fax: 503-494-4253; E-mail: schedin@ohsu.edu; and Virginia F. Borges, University of Colorado Anschutz Medical Campus, 12801 East 17th Avenue, Room 8121, Mailstop 8711, Aurora, CO 80045. Phone: 303-724-3888; E-mail: virginia.borges@ucdenver.edu

doi: 10.1158/2159-8290.CD-16-0822

©2016 American Association for Cancer Research.

promotes the early stages of breast cancer metastasis, including tumor cell escape from the mammary gland (4–6). However, late stages of the metastatic cascade are rate limiting, including survival at secondary sites (7), and highlight the critical role of the “soil” in determining the fate of the metastatic “seed.” For example, in experimental metastasis models, tumor cells extravasate into secondary tissues at high rates but subsequently die off or fail to efficiently establish overt metastatic lesions (7). Prometastatic microenvironments can shift this bottleneck such that tumor cells are more likely to successfully establish metastatic lesions (8–10). Here, we tested whether breast cancer cells have a metastatic advantage at secondary sites in the postpartum host. The rationale for this hypothesis is based upon the assumption that organs with increased metabolic output during pregnancy and lactation, such as the liver, might undergo postpartum involution to return the organ to its baseline metabolic state. This tissue involution process is anticipated to enhance metastasis, as physiologic tissue involution is mediated by wound healing-like programs known to support tumor growth (5, 6). Here, using rodent models, we report that pup weaning induces maternal liver involution characterized by hepatocyte cell death and stromal remodeling consistent with establishment of a prometastatic microenvironment. Experimental metastasis models demonstrate increased liver metastasis in post-weaning mice compared with nulliparous hosts. Potential human significance is suggested by a preferential increase in liver metastasis in postpartum patients compared with nulliparous controls. In summary, our studies identify a heretofore-unrecognized biology of the rodent liver, weaning-induced liver involution, a tissue remodeling process that establishes a prometastatic microenvironment. These findings address the role of normal physiology on metastatic niche education in the absence of a primary tumor and provide a novel mechanism that may explain poor outcomes of patients with postpartum breast cancer.

RESULTS

Dynamic Regulation of the Rodent Liver during Pregnancy, Lactation, and Weaning

Evidence for weaning-induced involution in tissues other than the breast has not been reported. We focused on the liver, which increases in metabolic output during pregnancy and lactation (11, 12). Specifically, the liver increases lipid β -oxidation to facilitate production of glucose that is shuttled to the mammary gland for milk production (13, 14). Yet how the liver returns to its baseline metabolic state after weaning is unknown. To begin to address this question, we performed a pregnancy and weaning study in Sprague Dawley female rats (Fig. 1A). We found rat liver weights increased ~2-fold during pregnancy and remained elevated during lactation (Fig. 1B; Supplementary Fig. S1A). We also observed that liver weights rapidly returned to nulliparous levels by 8 to 10 days after weaning, data consistent with weaning-induced liver involution (Fig. 1B). In contrast, lung weights did not change with parity, lactation, or weaning status (Supplementary Fig. S1B).

To assess if the rapid liver weight loss after weaning is due to hepatocyte cell death, we first investigated whether hepatocyte proliferation contributed to liver weight gain during pregnancy. We reasoned that if liver weight gain during pregnancy involved new cell proliferation, then resolution of weight gain

may be mediated by cell removal, i.e., hepatocyte cell death. During pregnancy, we found increased hepatocyte proliferation, as measured by elevated Ki67 positivity and mitotic figures (Fig. 1C; Supplementary Fig. S1C and S1D). During lactation, a modest increase in liver weight gain over pregnancy was associated with hepatocyte hypertrophy (Supplementary Fig. S1E). In addition, hepatocyte hypertrophy correlated with an anabolic metabolome profile, consistent with the increased metabolic demand of lactation (Fig. 1D; Supplementary Table S1A; refs. 13 and 14). Conversely, the post-weaning liver exhibited metabolic signatures of nucleic acid and protein catabolism and oxidative stress (Fig. 1D; Supplementary Table S1A). Performing supervised clustering [partial least squares discriminant analysis (PLS-DA)] of the rat liver metabolomics data revealed a step-wise, cyclical metabolic pattern across the reproductive cycle (Fig. 1E; see Supplementary Methods). These data are consistent with dramatic functional changes to accommodate lactation, and further demonstrate a return to a nulliparous-like, baseline state upon regression at 28 days after weaning (Fig. 1E). The drop in liver weight and metabolic shift of the liver after weaning is accompanied by increased detection of cleaved caspase-3 (CC3; Fig. 1F; Supplementary Fig. S1F), data suggestive of apoptotic cell death and tissue regression. Further evidence for weaning-induced hepatocyte cell death was observed by increased terminal deoxynucleotidyl transferase dUTP nick end labeling (TUNEL) staining, which labels cleaved DNA (Fig. 1G; Supplementary Fig. S1G). Combined, our data confirm and expand on previous studies demonstrating that hepatocyte proliferation and anabolic metabolism occur to accommodate the energy demands of lactation (12, 13). Our data also show, for the first time, that weaning induces rapid hepatocyte cell death and liver involution, returning the liver to a baseline size and metabolic state within two weeks of weaning. We next addressed whether stromal remodeling accompanies weaning-induced liver involution, as stromal remodeling is known to affect breast cancer metastasis (9, 10, 15).

Weaning-Induced Liver Involution Is Accompanied by Stromal Remodeling

We turned to the extensively investigated post-weaning mammary gland model to guide our investigation of stromal changes that occur in the actively involuting liver (16), as extracellular matrix (ECM) remodeling is a defining characteristic of the post-weaning mammary gland (4, 17, 18). Quantitative ECM proteomics on the rat liver revealed widespread changes in ECM proteins post-weaning (Fig. 2A; Supplementary Table S1B). Similar to our findings from the metabolomics analysis, supervised clustering (PLS-DA) of the ECM proteomic dataset demonstrated distinct liver ECM microenvironments across the reproductive cycle, including resolution to nulliparous-like composition in the fully regressed liver (R; Fig. 2B; Supplementary Fig. S2). During the active window of liver involution, we found elevated collagen 1- α 1, collagen 4- α 1, and tenascin-C (TNC; Fig. 2C; Supplementary Fig. S3A and S3B), ECM proteins upregulated in the involuting mammary gland (17) as well as in prometastatic microenvironments (9, 10, 15, 19). Increased transcript levels for *COL1A1* and *TNC* suggested active ECM production in the involuting liver (Supplementary Fig. S3C), and quantitative reticulin staining (Supplementary

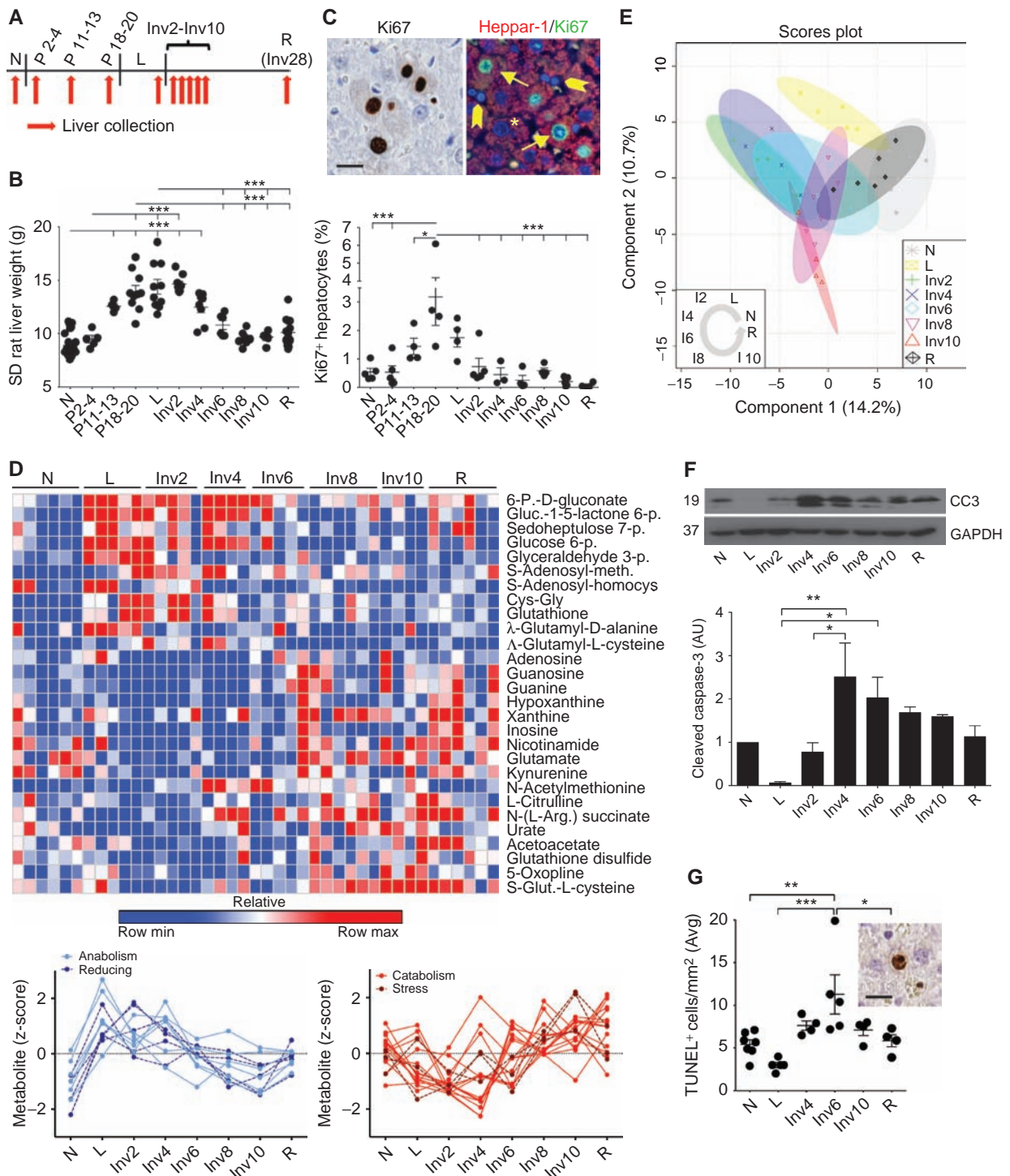


Figure 1. Evidence for weaning-induced liver involution. **A**, Rat livers were harvested for biochemical and IHC analyses (red arrows) from nulliparous (N), early (P2-4), mid (P11-13), and late (P18-20) pregnancy, lactation day 10 (L), and post-weaning days 2-10 and 28 (Inv2-Inv10, R). **B**, Liver weights from age-matched rats across the reproductive cycle; rats/group: Nullip (N), $n = 25$; P2-4, $n = 5$; P11-13, $n = 4$; P18-20 and L, $n = 10$; Inv2, $n = 9$; Inv4, $n = 8$; Inv6 and Inv10, $n = 6$; Inv8, $n = 7$; Regressed (R), $n = 14$. **C**, Representative Ki67 IHC (top left) and dual Ki67/Heppar-1 IHC (top right) images from P18-20 liver; Ki67+ hepatocytes (arrows); Ki67+ nonparenchymal cells (asterisk); Ki67+ nonparenchymal cells (arrowheads); scale bar, 20 μm . Quantification of Ki67+ hepatocyte IHC by reproductive stage (bottom); $n = 4$ rats/group. **D**, Heat map of UHPLC-MS metabolomics by reproductive stage (top) and z-scores of anabolic/reducing (bottom left) and catabolic/stress (bottom right) metabolites; $n = 4-6$ rats/group. **E**, Partial least squares discriminate analysis (PLS-DA) of rat liver metabolomics data (see Supplementary Table S1A). **F**, Cleaved caspase-3 immunoblot (top; $n = 4$ rats/group) and densitometry (bottom). **G**, Representative apoptotic hepatocyte detected by TUNEL (inset; scale bar, 20 μm), and TUNEL quantification across the reproductive cycle; N, $n = 7$; L and Inv6, $n = 5$; Inv4, Inv10, and R, $n = 4$. Graphs show mean with SEM. One-way ANOVA with the Tukey multiple comparisons test. *, $P < 0.05$; **, $P < 0.01$; ***, $P < 0.001$.

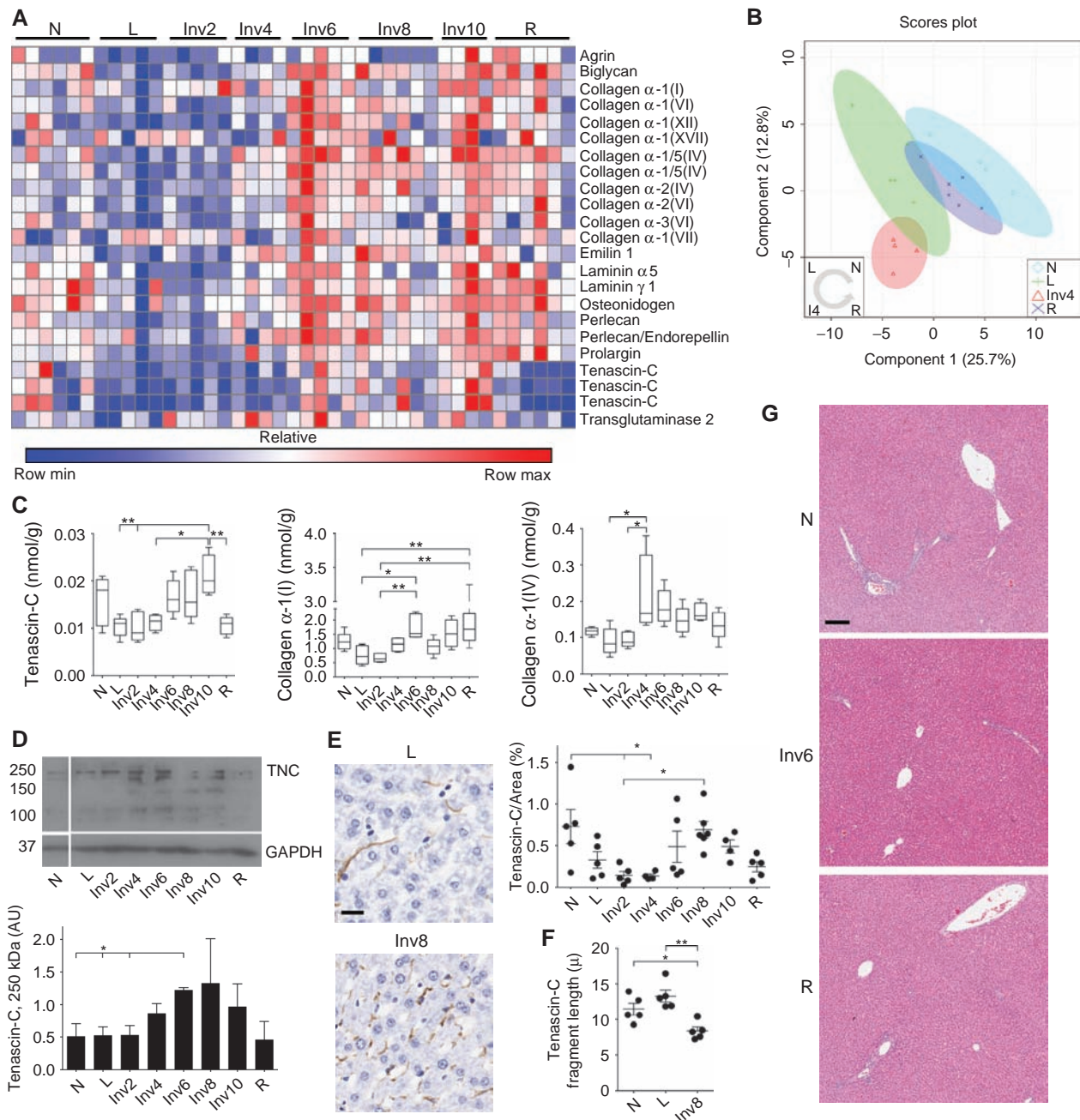


Figure 2. ECM remodeling accompanies weaning-induced liver involution. **A**, Absolute quantification of rat liver ECM proteins by QconCAT-based MS/MS proteomics; $n = 4-6$ rats/group. **B**, Partial least squares discriminate analysis (PLS-DA) of rat liver ECM proteomics data from N, L, Inv6, and R stages (see Supplementary Fig. S2 and Supplementary Table S1B). **C**, Box and whisker plots of TNC, collagen 1- α 1, and collagen 4- α 1 obtained from QconCAT proteomics in **A**. **D**, TNC expression across involution by immunoblot (top, and Supplementary Fig. S3E), with densitometry normalized to GAPDH (bottom, and Supplementary Fig. S3E); quantification is of 4 technical replicates, $n = 4-6$ rats/group. **E**, Representative liver TNC IHC (brown stain) at L (top left) and Inv8 (bottom left) and IHC quantification across reproductive stage (top right); scale bar, 25 μ m; $n = 4-6$ rats/group. **F**, TNC fragment length measured in N, L, and Inv8 livers; $n = 5$ rats/group. **G**, Representative hematoxylin and eosin-stained rat liver sections from N (top), Inv6 (middle), and R (bottom) stages; scale bar, 150 μ m. Graphs show mean with SEM. One-way ANOVA with the Tukey multiple comparisons test. *, $P < 0.05$; **, $P < 0.01$.

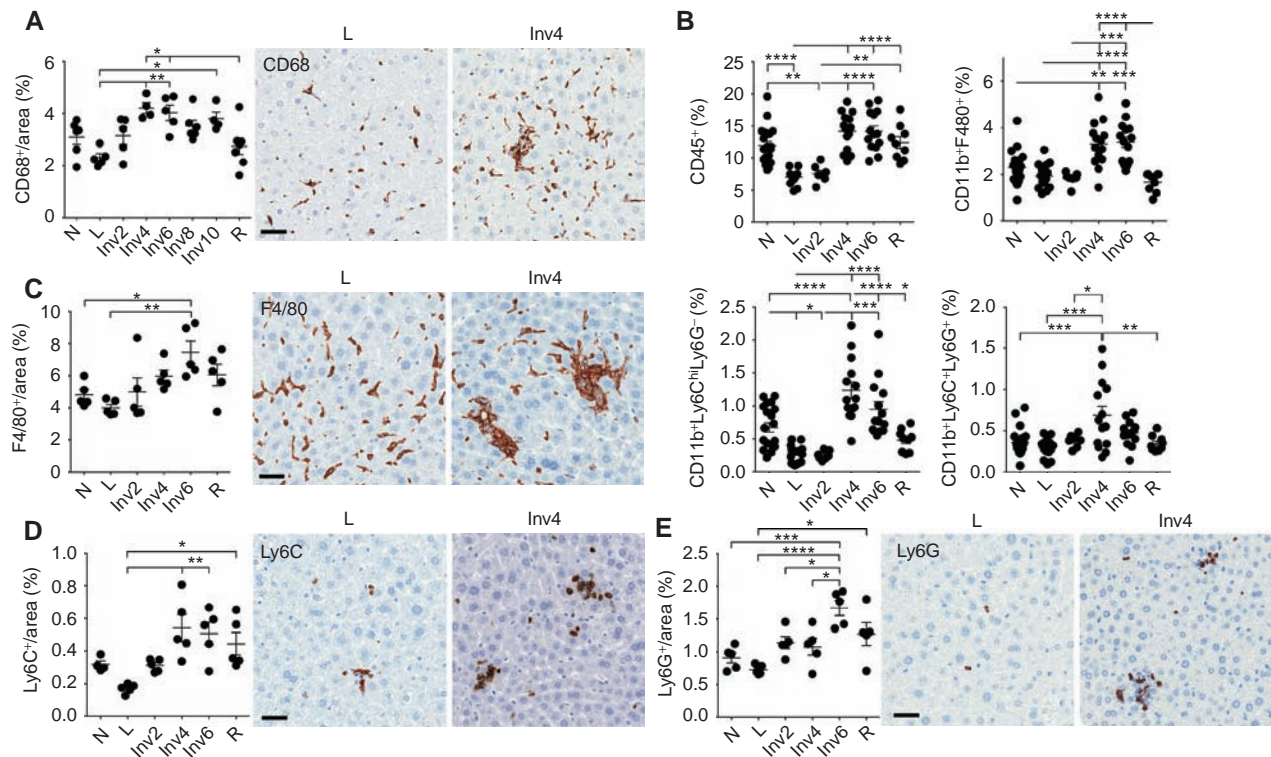


Figure 3. Immune populations increase in the liver during weaning-induced involution. **A**, IHC quantification of CD68 positivity (left) and representative CD68 IHC images (right); scale bar, 40 μ m; $n = 4$ –6 rats/group. **B**, Flow-cytometric quantification of BALB/c mouse liver immune cell populations; CD45⁺ leukocytes (top left), CD11b^{hi}F4/80⁺Ly6C⁻Ly6G⁻ mature macrophages (top right), CD11b^{hi}F4/80⁻Ly6C⁺Ly6G⁻ monocytes (bottom left), and CD11b^{hi}F4/80⁻Ly6C⁺Ly6G⁺ neutrophils (bottom right); Nullip (N), $n = 19$; L, Inv4, and Inv6, $n = 14$; R, $n = 9$; Inv2, $n = 7$ mice/group. **C**, F4/80 IHC quantification (left), and representative F4/80 IHC images (right); $n = 5$ mice/group. **D**, Ly6C IHC quantification (left), and representative Ly6C IHC images (right); $n = 5$ mice/group. **E**, Ly6G IHC quantification (left), and representative Ly6G IHC images (right); scale bars for **C**–**E**, 40 μ m; $n = 5$ mice/group. Graphs show mean with SEM. One-way ANOVA with the Tukey multiple comparisons test. *, $P < 0.05$; **, $P < 0.01$; ***, $P < 0.001$; ****, $P < 0.0001$.

Fig. S3D), TNC immunoblot (Fig. 2D; Supplementary Fig. S3E), and TNC immunostaining (Fig. 2E; Supplementary Fig. S3F) confirmed increased collagen and TNC protein deposition within the post-weaning liver. Of note, the timeline of TNC protein accumulation differs slightly by assay, and although these apparent discrepancies remain to be resolved, all three assays support increased liver ECM deposition shortly after weaning. Additionally, shorter TNC fragments were observed after weaning (Fig. 2D–F; Supplementary Fig. S3F), and gelatin zymography demonstrated increased MMP9 and MMP2 levels (Supplementary Fig. S3G), data supportive of active ECM remodeling in the post-weaning liver, as observed in the involuting mammary gland (5, 17, 18). Although hepatocyte cell death and ECM deposition also occur in pathologic liver injury, the ECM deposition observed during weaning-induced liver involution occurred in the absence of overt fibrosis (Fig. 2G; Supplementary Fig. S3H). Taken together, these data show active, cyclical, physiologic ECM remodeling during the window of weaning-induced liver involution.

Immune Cell Accumulation during Weaning-Induced Liver Involution

Immune cell infiltrate is another defining stromal change in the involuting mammary gland (6) and was suggested in the involuting rat liver by increased CD68 staining, a macrophage

lysosomal marker (Fig. 3A). To further investigate the immune milieu in the post-weaning liver, we turned to the BALB/c murine model, which permits robust immune cell characterization by flow cytometry. We first confirmed murine hepatocyte proliferation and liver weight gain during pregnancy, followed by liver weight loss, metabolic catabolism/stress, and increased apoptosis upon weaning (Supplementary Fig. S4A–S4D; Supplementary Table S2). Increased TNC, MMP9, and MMP2 in the post-weaning mouse liver provided further evidence that weaning-induced liver involution is conserved between rats and mice (Supplementary Fig. S4E–S4H). In mice, liver immune cell phenotyping by flow cytometry revealed transient increases in CD45⁺ leukocytes, CD11b^{hi}F4/80⁺ macrophages, CD11b^{hi}F4/80⁻Ly6C⁺Ly6G⁻ monocytes, and CD11b^{hi}F4/80⁻Ly6C⁺Ly6G⁺ neutrophils with weaning (Fig. 3B; Supplementary Fig. S5A and S5B). Semiquantitative IHC detection of F4/80⁺, Ly6C⁺, and Ly6G⁺ cells confirmed a transient increase in macrophages, monocytes, and neutrophils in the post-weaning liver (Fig. 3C–E). The observed influx of myeloid populations during weaning-induced liver involution may be, in part, due to increased production of chemokines. Thus, we looked at chemokines known to promote monocyte influx into tissues and found an increase in both *Cxcl12* and *Ccl2* expression during liver involution (Supplementary Fig. S5C–S5E). Additionally, previous work has reported

the formation of myeloid immune foci in the premetastatic niche (8), an observation we also report here (Supplementary Fig. S5F and S5G). Our finding of increased myeloid populations within the liver after weaning is also consistent with clearance of apoptotic cells and immune suppression. Specifically, professional phagocytic clearance of apoptotic cells limits exposure to self-antigen (20) and gives rise to immune-suppressive, wound-resolving macrophages (21) that support tumor cell immune evasion (22).

In sum, we provide evidence that the liver undergoes weaning-induced involution that is characterized by ECM deposition, MMP activity, and infiltration/clustering of CD11b^{hi}F4/80⁻Ly6C⁺Ly6G⁻ monocytes reported to occur within the metastatic niche as a result of primary tumor education (8–10, 23, 24). Our data indicate regulation of these same prometastatic pathways in the absence of tumors, under the physiologic conditions of weaning-induced liver involution. Based on these findings, we hypothesized that the post-weaning liver would preferentially support breast cancer metastasis in comparison with the nulliparous host.

Weaning-Induced Liver Involution Establishes a Prometastatic Microenvironment

To determine if the involuting liver supports metastasis to a greater extent than the nulliparous host liver, we injected 5,000 mammary 4T1 tumor cells into the left ventricle of isogenic BALB/c hosts that were nulliparous or immediate post-weaning, referred to as the involution group (Inv2; Fig. 4A). Intracardiac injection was necessary to ensure equal circulating tumor cell numbers in both groups, as we have previously shown increased tumor cell dissemination from the mammary fat pad during weaning-induced mammary gland involution (4, 5). At study end, the percentage of mice with tumor cells in the liver, as assessed by a clonogenic assay for 4T1 cells (25), was higher in the involution group, and cells were detected earlier in comparison with nulliparous hosts (Fig. 4B and C). The percentage of mice with tumor cells in the lung, bone, and brain was unchanged between groups, suggesting a unique metastatic advantage within the post-weaning liver (Fig. 4D). By immunohistochemical (IHC) assessment, liver metastases were confirmed as CD45⁻, Heppar-1⁻, and CK18⁺, and found to be highly Ki67 positive (Fig. 4E). Micrometastases were the dominant lesion type, likely due to the fact that systemic tumor burden and 4T1 tumor cell-driven cachexia required sacrifice of mice prior to the formation of overt liver metastasis.

To assess the ability of the post-weaning liver to support macrometastases, we developed a portal vein injection metastasis model that allows for tumor cell delivery directly to the liver. This model permits outgrowth of liver lesions without concomitant metastasis in other organs (26). Further, to avoid cachexia, we utilized the less aggressive, isogenic, murine D2A1 mammary tumor cell line. We delivered 5,000 D2A1 cells into the portal vein of nulliparous and immediate post-weaning BALB/c female mice (Fig. 4F). This cell number was selected to reduce penetrance of overt liver lesions in nulliparous mice to ~20% (data not shown), permitting detection of a potential increase in metastatic frequency in the involution group. To investigate whether the prometastatic microenvironment of the post-weaning liver is transient or persistent, we also injected mice at 28 days after weaning, a time point where

the liver is fully regressed (R) by morphologic, molecular, and biochemical characterizations (Figs. 1E and 2B; Supplementary Fig. S2 and Supplementary Table S3). In the immediate post-weaning group (Inv2), we observed a 3-fold increased frequency of histologically identified overt liver metastases compared with both nulliparous and fully regressed groups (Fig. 4G). By IHC, D2A1 liver lesions were identified as Heppar-1⁻, CK18⁺, and CD45⁻ and found to be highly positive for Ki67 (Fig. 4H; Supplementary Fig. S6).

To assess for differences in metastatic burden across groups, we quantified tumor number and size from hematoxylin and eosin (H&E) liver sections. From this analysis, we found that the immediate post-weaning (Inv2) group had an increased number of tumors per liver and increased tumor burden measured as total tumor area per liver, compared with the nulliparous group (Supplementary Fig. S7A and S7B). However, when we assessed only those mice with detectable metastases, differences in tumor number and area were not observed between groups (Supplementary Fig. S7C–S7E). Cumulatively, these data indicate that the window of increased risk for developing liver metastasis is transient, limited to the period of active liver involution following weaning. Further, data from this metastasis model suggest that liver involution supports the early event of tumor cell seeding, but not tumor growth. Finally, these data predict increased liver metastasis in women diagnosed with postpartum breast cancer.

Evidence for Elevated Risk for Liver Metastasis in Patients with Postpartum Breast Cancer

To investigate liver metastasis in young women with breast cancer, we evaluated a unique cohort of 564 patients diagnosed at ≤45 years of age where specific clinical data not normally collated, including parity history, long-term follow-up, and sites of metastasis, were made available through detailed chart review (Supplementary Table S4). Compared with nulliparous women, we found a ~3.6-fold increase in liver metastasis in postpartum patients diagnosed within 5 years of giving birth, a trend that continued for up to 10 years following parturition (Fig. 4I). This increased risk for liver metastasis persisted after adjusting for tumor biologic subtype, patient age, and year of diagnosis, which accounts for treatment advances over time (Supplementary Tables S4 and S6). To examine potential breast cancer preference for the postpartum liver, we next investigated site-specific metastasis in the subset of women with metastatic disease. To more accurately evaluate metastatic tropism to the postpartum liver, we restricted our analysis to cases where first site of metastasis was recorded. This approach would avoid potential confounding influences that concomitant multi-site metastasis might have on the liver metastatic niche. To increase the sample size of this highly defined young women's breast cancer cohort, we extended our analysis to multiple institutions where *de novo* and recurrent metastatic disease data were available and expanded the cohort to include patients diagnosed within 10 years of pregnancy (Supplementary Table S5). In this metastatic patient cohort, we observed increased liver metastasis in postpartum patients compared with nulliparous breast cancer patients (Fig. 4J). This increase appears to be liver specific, as we did not observe significant differences in frequencies of lung or brain metastasis between

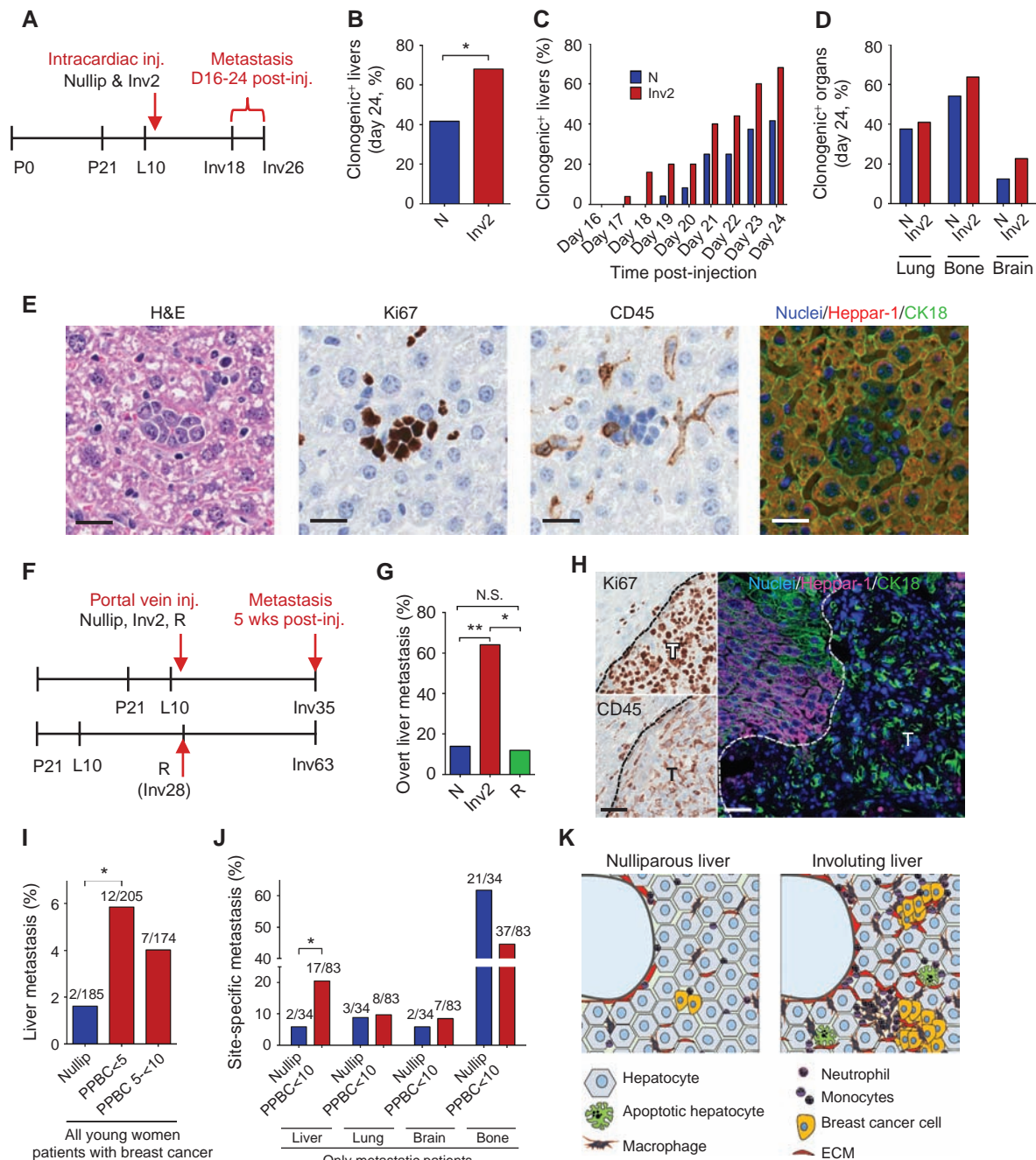


Figure 4. Evidence for a prometastatic microenvironment in the postpartum liver. **A**, Intracardiac metastasis model, Nullip (N), $n = 24$; Inv2, $n = 25$. **B**, Percentage of mice with tumor cells in liver [$P = 0.03$; χ^2 , RR 1.6 (95% CI, 0.9–9.6)]; **C**, Tumor cell latency. **D**, Percentage of mice with tumor cells in lung ($P = 0.81$), bone marrow ($P = 0.51$), and brain ($P = 0.36$). **E**, Representative H&E image of liver micrometastasis and staining for Ki67, CD45, and Heppar-1/CK18; scale bars, 25 μm . **F**, Portal vein metastasis model, Nullip, $n = 18$; Inv2, $n = 17$; R, $n = 8$. **G**, Percentage of mice with overt metastasis at study end [**, $P = 0.001$, RR 3.9 (95% CI, 1.3–11.6); *, $P = 0.03$, RR 2.0 (1.08–3.66)]; two-tailed Fisher exact test]. **H**, Representative Ki67, CD45, and Heppar-1/CK18 staining on overt liver metastases (T) from Inv2 mice, dashed lines denote tumor border; scale bars, 25 μm . **I**, Frequency of liver metastasis in young patients with breast cancer (≤ 45 years of age); N, $n = 185$; PPBC < 5, $n = 205$; PPBC 5–<10, $n = 174$ [*, $P = 0.038$; multivariate logistic regression, OR = 4.05 (95% CI, 1.08–15.12)]. **J**, Subset analysis of site-specific metastases in women with metastatic disease (N, $n = 34$; PPBC < 10, $n = 83$). Frequency of liver metastasis [*, $P = 0.04$, one-sided Fisher exact test; $P = 0.058$, two-sided Fisher exact test, OR: 4.12 (95% CI, 0.90–18.94)] and lung ($P = 1.00$), brain ($P = 1.00$), and bone ($P = 0.11$) metastasis by Fisher exact test (see Supplementary Table S6). **K**, Model of the postpartum involuting liver prometastatic microenvironment.

groups (Fig. 4J; Supplementary Tables S5 and S6). Intriguingly, we observed a trend toward reduced frequency of bone metastasis in the postpartum patients (Fig. 4J; Supplementary Tables S5 and S6). Cumulatively, these data support the hypothesis that the microenvironment of the postpartum involuting liver is uniquely permissive for the formation of breast cancer metastasis (Fig. 4K).

DISCUSSION

We provide the first description of a developmentally regulated, liver involution program induced by weaning, a program that returns the liver from a state of high metabolic output necessary for lactation to a baseline pre-pregnant-like state. Weaning-induced liver involution involves liver weight loss, hepatocyte apoptosis, catabolic and cell stress metabolite profiles, ECM deposition, and increases in myeloid populations associated with apoptotic cell clearance and immune suppression. Using intracardiac and intraportal tumor cell injection models of breast cancer metastasis, we found the actively involuting murine liver supports increased metastasis compared with the livers of nulliparous or postpartum hosts whose livers have completed the involution process, i.e., regressed hosts. Potential relevance to patients with breast cancer is suggested by our observation that patients diagnosed postpartum experience an elevated risk for liver-specific metastasis when compared with nulliparous young women with breast cancer. Unresolved by our studies is a reconciliation between the narrow window of increased risk for liver metastasis observed in the murine model and the extended window of risk observed in women (5–10 years postpartum). One possible mechanism for this potential timing discrepancy is through dissemination of breast cancer cells shortly after pregnancy/lactation, as previously proposed (5), followed by a dormancy phase prior to metastatic expansion.

Although physiologically regulated, the tissue-remodeling attributes of weaning-induced liver involution, including TNC, collagen I, collagen IV, and MMPs, are identified as key components of primary tumor-educated metastatic niches (8–10, 15, 23, 24). For example, breast cancer cells depend upon TNC for successful establishment of lung metastasis in mice (10), and collagen I at secondary sites can promote tumor cell escape from dormancy through integrin-mediated cytoskeletal rearrangement and proliferation (15). In addition, cross-linked collagen IV supports immune cell infiltration, production of MMP2 by monocytes, and metastatic niche formation in the murine lung, brain, and liver, ultimately facilitating tumor cell recruitment and metastatic outgrowth (9). We also observed increased CD11b⁺ myeloid cell infiltrate in the involuting liver, and previous work has shown that CD11b⁺ bone marrow-derived monocytes (BMDM) are essential for the establishment of successful metastasis upon tumor cell arrival in the liver (24). Similarly, seminal work has revealed that VEGFR1⁺ BMDM, a subset of which are CD11b⁺, are “first responders” in the premetastatic niche, where they are implicated in establishing a prometastatic environment hospitable to circulating tumor cells (8). The identification of several components of the tumor-educated metastatic niche within the normal involuting liver provides mechanistic support for our functional data demonstrating

increased liver metastasis in post-weaning compared with nulliparous murine hosts.

A limitation of our study is that we have yet to demonstrate causality between weaning-induced liver involution and increased metastasis. Such assessments will require abrogation of these involution-related prometastatic attributes by use of targeted interventions as well as genetic approaches. An additional constraint of our study is the use of metastasis models that do not recapitulate the entire metastatic cascade, but rather focus on the fate of circulating tumor cells. However, our reductionist approach is essential to isolate postpartum liver biology from that of the mammary gland, as previous studies in our lab revealed a metastatic advantage of orthotopic tumors in postpartum hosts, including increased tumor growth, local invasion, and escape into the circulation (5, 6).

The highly novel aspect of our discovery of weaning-induced liver involution and establishment of a transient prometastatic niche in rodents is also a potential limitation, as relevance to women is unknown. Our observations are unprecedented and, to date, no published studies have examined whether weaning-induced liver involution occurs in women. Such investigation will require noninvasive, serial liver imaging studies in pregnant, lactating, and post-weaning women. Studies using nonhuman primates, where liver biopsy is a viable option, could provide information regarding the molecular mechanisms of postpartum liver involution. Of potential significance, postpartum breast involution in women occurs to a similar degree and by many of the same physiologic processes as found in rodents, revealing conservation of weaning-induced breast involution (27).

Importantly, in a retrospective study of young women with breast cancer, we find postpartum patients are at increased risk for liver metastasis; these data are consistent with an unrevealed postpartum liver biology in women. Of note, we observe increased liver metastasis without observing differences in frequency of other common sites of breast cancer metastasis, including bone, lung, and brain; these data are suggestive of a liver-specific metastatic advantage. Independent validation of increased site-specific liver metastasis in patients with postpartum breast cancer is needed. Such studies will depend upon the expansion of young women’s breast cancer cohorts worldwide, as it is necessary to include time since last pregnancy histories, as well as sites of metastases; these clinical parameters are not routinely collected at present. Of note, we find the increased risk of liver metastasis persists beyond the predicted window of weaning-induced tissue involution, for up to 10 years postpartum. To test the speculation that postpartum breast involution facilitates early dissemination to the liver, prior to a diagnosis of breast cancer, new breast cancer models are needed.

In conclusion, we find an increase in site-specific metastasis to the liver in postpartum patients and identify weaning-induced liver involution in rodents as a putative mechanism that may account for this increased risk. Importantly, patients with breast cancer liver metastasis have a median survival of ~4 months, compared with ~5 years with bone-only metastasis (28, 29), raising the possibility that differences in site-specific metastasis contribute to the poor survival rates of women diagnosed postpartum. If validated, our finding that postpartum patients

experience an increased risk for liver metastasis could lead to changes in treatment decisions in this vulnerable population of young mothers diagnosed with breast cancer. Finally, our study implicates unique host biology, rather than intrinsic attributes of the tumor, in mediating the poor prognosis of postpartum breast cancer and offers unexplored avenues for metastasis research and therapeutic intervention.

METHODS

Postpartum Rodent Models

The University of Colorado Anschutz Medical Campus and Oregon Health & Science University (OHSU) Institutional Animal Care and Use Committees approved animal procedures. Age-matched female Sprague-Dawley rats (Harlan) and BALB/c mice (Jackson Laboratories, Bar Harbor, ME) were housed and bred as described (4, 6). For tissue collection, rodents were euthanized across groups either by CO₂ asphyxiation or while under anesthesia by exsanguination via portal vein perfusion with PBS. Whole livers and/or lungs were removed, washed 3× in 1× PBS, and weighed. Median and right liver lobes were digested for flow cytometry analyses, left lobes were fixed in 10% neutral buffered formalin (Anatech Ltd.), and caudate lobes were flash frozen on liquid nitrogen for protein and RNA extraction.

Cell Culture

4T1 cells, provided by Dr. Heide Ford in 2011 (University of Colorado, Aurora, CO), were cultured as described (25). D2A1 cells were a gift from Dr. Ann Chambers in 2011 (London Health Sciences Centre, London, Ontario) and were cultured as described (30). Cells were washed and resuspended in cold 1× PBS (Corning) for intracardiac and portal vein injections. The 4T1 and D2A1 cells were confirmed murine pathogen and *Mycoplasma* free, with a last testing date of March 28, 2011 (IDEXX BioResearch). Cell lines have not been authenticated. All cells used in the described experiments were within 2 to 5 passages of the tested lot.

Intracardiac Model of Metastasis

Anesthetized mice (2% isoflurane) with thoracic cavity hair removed with chemical depilatory were imaged using a Vevo 770 High-Resolution *In Vivo* Micro-Imaging System (Visual Sonics) and a 35-MHz mechanical transducer. Five thousand 4T1 isogenic mammary tumor cells/100 μL PBS were loaded in a 1 mL syringe with a 30-gauge 1" needle and the needle tip rinsed with sterile saline to remove external tumor cells. Under ultrasound image guidance, the needle was placed into the left ventricle, tumor cells were injected, and the needle was held within the heart for 4 to 6 seconds to ensure tumor cells entered the circulation. Nulliparous and involution day 2 mice were alternately injected. Mice were weighed daily and euthanized in a rolling study design, in pairs, one/group, upon weight loss (10%–15% of body weight). All mice were euthanized 16 to 24 days after injection (Nullip, *n* = 24; Inv2, *n* = 25). The presence of 4T1 tumor cells in the liver, lung, bone, and brain was determined using clonogenic assays (25). Mice were excluded if thoracic tumors were evident.

Intraportal Injection Model of Metastasis

Mice were anesthetized, abdominal hair removed, and 5,000 D2A1 isogenic mammary tumor cells/10 μL PBS injected into the portal vein as described (26). Mice were euthanized at 5 weeks after injection (Nullip, *n* = 18; Inv2, *n* = 17; R, *n* = 8) and visible liver metastasis assessed at necropsy. Five mice had equivocal liver lesions <3 mm in diameter that were subsequently assessed by histologic evaluation of H&E thin sections by a pathologist blinded to group. Of these mice, four had overt metastasis. Data are presented as the percentage of mice in each group with liver metastasis.

Flow Cytometry

For initial flow-cytometric analyses, individual mouse livers were digested in 1 mg/mL collagenase I and 0.5 mg/mL hyaluronidase for 30 minutes of shaking at 37°C, and filtered through a 100-μm filter (BD Biosciences). Red blood cells were lysed using 1× RBC lysis buffer (eBioscience). Samples were washed 3× with 1× PBS and counted in trypan blue using a Cellometer T4 Plus Cell Counter (Nexcelom Bioscience). Cells (1 × 10⁶) per sample were blocked with CD16/32 (eBioscience, 1:100) for 30 minutes and cell surface markers were stained (CD45, 30-F11; CD11b, M1/70; F4/80, CI:A3-1; Ly6C, HK1.4; Ly6G, 1A8) for 35 minutes at 4°C in 100 μL FACS buffer and fixed with fixation buffer (BD Biosciences) for 30 minutes. Samples were analyzed on a Gallios 561 flow cytometer (Beckman Coulter; University of Colorado Flow Cytometry Core) and data analysis was done using Kaluza v1.2 software (Beckman Coulter). Single-color controls were used with each run and fluorescence-minus-one and isotype controls were used to confirm CD11b⁺, F4/80⁺, Ly6C⁺, and Ly6G⁺ populations. Secondary analyses (Supplementary Fig. S5) were performed after portal vein perfusion of livers with 1 × PBS, and Fixable Live-Dead Aqua (Invitrogen, Thermo Fisher; 1:250) was included with the CD16/32 block. This analysis was performed on an LSRFortessa (BD Biosciences; Oregon Health and Science University Flow Cytometry Shared Resource), and analysis was performed using FlowJo (FlowJo, LLC Data Analysis Software).

Metabolomics

For rat liver metabolomics, mass spectrometry was performed on *n* = 4 Inv4, Inv10; *n* = 5 L, Inv2, Inv6; and *n* = 6 N, Inv8, R rats/group. For mouse liver metabolomics, mass spectrometry was performed on *n* = 6 N, L, Inv2, Inv4, Inv6; *n* = 5 R; and *n* = 4 Inv8 mice/group. Pulverized rat or mouse liver tissues were suspended at 10 mg/mL in ice-cold lysis/extraction buffer (methanol:acetonitrile:water, 5:3:2), vortexed for 30 minutes at 4°C, and centrifuged at 10,000 × *g* for 15 minutes at 4°C. For LC/MS analysis, 10 μL of samples were injected into an ultra high-performance liquid chromatography (UHPLC) system (Ultimate 3000, Thermo Fisher) and run on a Kinetex XB-C18 column (2.1 × 150 mm i.d., 1.7-μm particle size, Phenomenex) using a 3-minute isocratic run at 250 μL/min (mobile phase: 5% acetonitrile, 95% 18 mΩ H₂O, 0.1% formic acid). The UHPLC system was coupled online to a Q Exactive mass spectrometer (Thermo Fisher), scanning in Full MS mode (2 μscans) at 70,000 resolution in the 60 to 900 *m/z* range, 4 kV spray voltage, 15 sheath gas, and 5 auxiliary gas, operated in negative and then positive ion mode (separate runs). Calibration was performed before each analysis using positive and negative ion mode calibration mixes (Pierce, Thermo Fisher) to ensure sub-ppm error of the intact mass. Metabolite assignments were performed using the software Maven (31), upon conversion of .raw files into .mzXML format through MassMatrix. The software allows for peak picking, feature detection, and metabolite assignment against the KEGG pathway database. Assignments were further confirmed using chemical formula determination from isotopic patterns and accurate intact mass, and by matching retention times to an in-house library that contains 650+ metabolites (Sigma-Aldrich and IROATech). Relative quantitation was performed by exporting integrated peak area values into Excel (Microsoft) for statistical analysis, including hierarchical clustering analysis (GENE-E; Broad Institute, Cambridge, MA). The metabolomics data reported in this article are tabulated in the supplementary materials and archived at The Metabolomics Consortium Data Repository and Coordinating Center (DRCC; Project ID PR000382: Rat metabolomics study ST000509, mouse metabolomics study ST000510).

Proteomics

For rat liver proteomics, mass spectrometry was performed on *n* = 4 Inv4, Inv10; *n* = 5 L, Inv2, Inv6; and *n* = 6 N, Inv8, R rats/group.

Approximately 50 mg of flash-frozen, pulverized liver tissue was processed as described (18, 32). The endogenous protein concentration of each sample was determined by the Bradford assay, prior to proteolytic digestion. Samples were digested using the FASP protocol (33). Briefly, 37.5 μ g of each sample was added to a 10-kD molecular weight cutoff filter. $^{13}\text{C}_6$ labeled ECM-associated QconCAT standards (500 fmols; ref. 32) were spiked into each sample. Samples were analyzed on the QTRAP 5500 triple quadrupole mass spectrometer (AB SCIEX) coupled with a UHPLC system (Ultimate 3000, Thermo Fisher). A targeted, scheduled Selected Reaction Monitoring (SRM) approach was performed using the QTRAP 5500. Each sample (16 μ L) was injected and directly loaded onto a Waters UPLC column (ACQUITY UPLC BEH C18, 1.7 μ m 150 \times 1 mm) with 5% acetonitrile (ACN), 0.1% formic acid at 30 μ L/min for 3 minutes. A gradient of 2% to 28% ACN was run for 21 minutes to differentially elute QconCAT peptides. The mass spectrometer was run in positive ion mode with the following settings: a source temperature of 200°C, spray voltage of 5300V, curtain gas of 20 psi, and a source gas of 35 psi (nitrogen gas). Transition selection and corresponding elution time, declustering potential, and collision energies were specifically optimized for each peptide of interest using Skyline's step-wise methods set-up (34). Method building and acquisition were performed using Analyst Software (Version 1.5.2).

Immunohistochemistry, immunofluorescence, staining analysis, immunoblot, zymography, and RNA analysis methodology are available in supplementary methods.

Statistical Analysis of Rodent Studies

All rodent data are from two independent breeding studies, with 4 to 25 animals per group, with the exception of immunoblots and zymogens, which were performed on pooled lysates with 4 samples/group run as 4 to 5 technical replicates. For intracardiac injection studies, a one-tailed χ^2 test was used to compare liver metastasis across groups based on preexisting hypotheses; a two-tailed χ^2 test was used to compare lung, bone, and brain metastasis. For portal vein injection studies, a two-sided Fisher exact test was used to compare frequency of liver metastasis across groups, and Student *t* test was used to compare number of lesions, lesion area, and tumor burden across groups. Statistical analyses were performed using GraphPad Prism 6. All data are presented with mean and standard error of the mean (SEM), where applicable.

Statistical Analysis of Patient Cohorts

The Colorado and OHSU Institutional Review Boards approved all human studies. All studies were conducted in accordance with the Declaration of Helsinki. Human subjects were enrolled via prospective trials where informed consent was obtained. University of Colorado (UC) cases before 2004 were obtained via consent and/or HIPAA-exempt approved retrospective protocol. Cohort demographic, clinical, and treatment data are summarized in Supplementary Tables S4 and S5, and data analyses are summarized in Supplementary Table S6. Two young women's breast cancer cohorts were analyzed, a UC cohort including all patients (≤ 45 years old) and a UC/Dana-Farber Cancer Institute (< 40 years old) cohort including only patients with metastatic recurrence. For analysis of the UC cohort ($n = 564$), patients were defined as nulliparous if they had no evidence of complete or incomplete pregnancy and as postpartum if they were diagnosed < 5 or $5 - < 10$ years after their last completed pregnancy. We excluded cases with incomplete parity data, if pregnant, or > 10 years postpartum at the time of diagnosis. Multivariate logistic regression was used to assess the effect of parity status on liver metastasis while adjusting for biologic subtype, age of the patient at diagnosis, and year of diagnosis. Patients in the subset analysis that included only metastatic patients ($n = 117$) were excluded if site of first metastatic recurrence was unknown, or if diagnosed with multisite metastatic disease upon initial

recurrence, to limit analysis to first site of metastasis. In this subset analysis, the association between liver metastasis and parity status was assessed using a one-sided (increased metastasis in the postpartum group was predicted) as well as a two-sided Fisher exact test, with significance ($P = 0.04$; one-sided) or a trend toward significance ($P = 0.058$; two-sided) demonstrated, respectively. The association between lung, bone, and brain metastasis and parity status was assessed using a two-sided Fisher exact test because we did not have a preexisting hypothesis.

Disclosure of Potential Conflicts of Interest

R.C. Hill is a managing partner at Omix Technologies. No potential conflicts of interest were disclosed by the other authors.

Authors' Contributions

Conception and design: P. Schedin, V.F. Borges, E.T. Goddard, O. Maller
Development of methodology: E.T. Goddard, R.C. Hill, T. Nemkov, A. D'Alessandro, K.C. Hansen, V.F. Borges, P. Schedin

Acquisition of data (provided animals, acquired and managed patients, provided facilities, etc.): E.T. Goddard, R.C. Hill, T. Nemkov, O. Maller, A.H. Partridge, V.F. Borges, P. Schedin

Analysis and interpretation of data (e.g., statistical analysis, biostatistics, computational analysis): E.T. Goddard, R.C. Hill, T. Nemkov, A. D'Alessandro, K.C. Hansen, S. Mongoue-Tchokote, M. Mori, V.F. Borges, P. Schedin

Writing, review, and/or revision of the manuscript: E.T. Goddard, R.C. Hill, K.C. Hansen, M. Mori, A.H. Partridge, V.F. Borges, P. Schedin

Administrative, technical, or material support (i.e., reporting or organizing data, constructing databases): V.F. Borges, P. Schedin

Study supervision: E.T. Goddard, V.F. Borges, P. Schedin

Acknowledgments

The authors would like to acknowledge the important scientific contributions of researchers whose work could not be cited due to space limitations. The authors would also like to thank the Schedin and Borges lab members Jacob Fischer, Sonali Jindal, Jeremy Johnston, Pat Bell, Hadley Holden, Marcella Brown, Jayasri Narasimhan, Breanna Caruso, Itai Meir, and Ethan Cabral for IHC and technical assistance and cohort data collection; Ana Coito (UCLA) for TNC knockout mouse tissue; Maria Cavin and the PreClinical Cardiovascular Core, UC Denver, for technical contributions to the intracardiac metastasis model; the UC Denver Flow Cytometry Shared Resource (NIH/NCI P30CA046934); the UC Denver Genomics and Microarray Core for RNA quality assessment; the OHSU Flow Cytometry Shared Resource (NIH/NCI P30CA069533); the OHSU Advanced Light Microscopy Core at the Jungers Center; Dexiang Gao of the Department of Pediatrics, School of Medicine at UC Denver for statistical analysis of the intracardiac metastasis data; and Lisa M. Coussens and Brian Ruffell for critical review of the manuscript. Finally, we are very grateful to the patients for their contributions to this research. The data reported here are tabulated in the article and supplementary materials and archived at The Metabolomics Consortium Data Repository and Coordinating Center (DRCC; Project ID PR000382: Rat metabolomics study ST000509, mouse metabolomics study ST000510).

Grant Support

Funding for this project includes NIH/NCI NRSA F31CA186524 (to E.T. Goddard); NIH/NCATS Colorado CTSI UL1 TR001082 for proteomic support and REDCap database support, NIH/NCIR33 CA183685 (to K.C. Hansen); DOD BC123567 (to P. Schedin); BC123567P1 (to K.C. Hansen); NIH/NCI R01CA169175 (to V.F. Borges and P. Schedin); and the Grohne Family Foundation.

Received July 25, 2016; revised December 8, 2016; accepted December 8, 2016; published OnlineFirst December 14, 2016.

REFERENCES

- Johansson AL, Andersson TM, Hsieh CC, Cnattingius S, Lambe M. Increased mortality in women with breast cancer detected during pregnancy and different periods postpartum. *Cancer Epidemiol Biomarkers Prev* 2011;20:1865–72.
- Callihan EB, Gao D, Jindal S, Lyons TR, Manthey E, Edgerton S, et al. Postpartum diagnosis demonstrates a high risk for metastasis and merits an expanded definition of pregnancy-associated breast cancer. *Breast Cancer Res Treat* 2013;138:549–59.
- Amant F, von Minckwitz G, Han SN, Bontenbal M, Ring AE, Giermek J, et al. Prognosis of women with primary breast cancer diagnosed during pregnancy: results from an international collaborative study. *J Clin Oncol* 2013;31:2532–9.
- McDaniel SM, Rumer KK, Biroc SL, Metz RP, Singh M, Porter W, et al. Remodeling of the mammary microenvironment after lactation promotes breast tumor cell metastasis. *Am J Pathol* 2006;168:608–20.
- Lyons TR, O'Brien J, Borges VF, Conklin MW, Keely PJ, Eliceiri KW, et al. Postpartum mammary gland involution drives progression of ductal carcinoma in situ through collagen and COX-2. *Nat Med* 2011;17:1109–15.
- Martinson HA, Jindal S, Durand-Rougely C, Borges VF, Schedin P. Wound healing-like immune program facilitates postpartum mammary gland involution and tumor progression. *Int J Cancer* 2015;136:1803–13.
- Luzzi KJ, MacDonald IC, Schmidt EE, Kerkvliet N, Morris VL, Chambers AF, et al. Multistep nature of metastatic inefficiency: dormancy of solitary cells after successful extravasation and limited survival of early micrometastases. *Am J Pathol* 1998;153:865–73.
- Kaplan RN, Riba RD, Zacharoulis S, Bramley AH, Vincent L, Costa C, et al. VEGFR1-positive haematopoietic bone marrow progenitors initiate the pre-metastatic niche. *Nature* 2005;438:820–7.
- Erler JT, Bennewith KL, Cox TR, Lang G, Bird D, Koong A, et al. Hypoxia-induced lysyl oxidase is a critical mediator of bone marrow cell recruitment to form the premetastatic niche. *Cancer Cell* 2009;15:35–44.
- Oskarsson T, Acharyya S, Zhang XH, Vanharanta S, Tavazoie SF, Morris PG, et al. Breast cancer cells produce tenascin C as a metastatic niche component to colonize the lungs. *Nat Med* 2011;17:867–74.
- Bustamante JJ, Copples BL, Soares MJ, Dai G. Gene profiling of maternal hepatic adaptations to pregnancy. *Liver Int* 2010;30:406–15.
- Milona A, Owen BM, van Mil S, Dormann D, Mataka C, Boudjelal M, et al. The normal mechanisms of pregnancy-induced liver growth are not maintained in mice lacking the bile acid sensor Fxr. *Am J Physiol Gastrointest Liver Physiol* 2010;298:G151–8.
- Rawson P, Stockum C, Peng L, Manivannan B, Lehnert K, Ward HE, et al. Metabolic proteomics of the liver and mammary gland during lactation. *J Proteomics* 2012;75:4429–35.
- Rudolph MC, McManaman JL, Phang T, Russell T, Kominsky DJ, Serkova NJ, et al. Metabolic regulation in the lactating mammary gland: a lipid synthesizing machine. *Physiol Genomics* 2007;28:323–36.
- Barkan D, El Touny LH, Michalowski AM, Smith JA, Chu I, Davis AS, et al. Metastatic growth from dormant cells induced by a col-I-enriched fibrotic environment. *Cancer Res* 2010;70:5706–16.
- Lund LR, Romer J, Thomasset N, Solberg H, Pyke C, Bissell MJ, et al. Two distinct phases of apoptosis in mammary gland involution: proteinase-independent and -dependent pathways. *Development* 1996;122:181–93.
- Schedin P, Mitrenga T, McDaniel S, Kaeck M. Mammary ECM composition and function are altered by reproductive state. *Mol Carcinog* 2004;41:207–20.
- Goddard ET, Hill RC, Barrett A, Betts C, Guo Q, Maller O, et al. Quantitative extracellular matrix proteomics to study mammary and liver tissue microenvironments. *Int J Biochem Cell Biol* 2016;81(Pt A):223–32.
- Burnier JV, Wang N, Michel RP, Hassanain M, Li S, Lu Y, et al. Type IV collagen-initiated signals provide survival and growth cues required for liver metastasis. *Oncogene* 2011;30:3766–83.
- Freire-de-Lima CG, Xiao YQ, Gardai SJ, Bratton DL, Schiemann WP, Henson PM. Apoptotic cells, through transforming growth factor-beta, coordinately induce anti-inflammatory and suppress pro-inflammatory eicosanoid and NO synthesis in murine macrophages. *J Biol Chem* 2006;281:38376–84.
- Ramachandran P, Pellicoro A, Vernon MA, Boulter L, Aucott RL, Ali A, et al. Differential Ly-6C expression identifies the recruited macrophage phenotype, which orchestrates the regression of murine liver fibrosis. *Proc Natl Acad Sci U S A* 2012;109:E3186–95.
- Cook RS, Jacobsen KM, Wofford AM, DeRyckere D, Stanford J, Prieto AL, et al. MerTK inhibition in tumor leukocytes decreases tumor growth and metastasis. *J Clin Invest* 2013;123:3231–42.
- Hiratsuka S, Nakamura K, Iwai S, Murakami M, Itoh T, Kijima H, et al. MMP9 induction by vascular endothelial growth factor receptor-1 is involved in lung-specific metastasis. *Cancer Cell* 2002;2:289–300.
- Zhao L, Lim SY, Gordon-Weeks AN, Tapmeier TT, Im JH, Cao Y, et al. Recruitment of a myeloid cell subset (CD11b/Gr1 mid) via CCL2/CCR2 promotes the development of colorectal cancer liver metastasis. *Hepatology* 2013;57:829–39.
- Pulaski BA, Ostrand-Rosenberg S. Mouse 4T1 breast tumor model. *Curr Protoc Immunol* 2001;Chapter 20:Unit 20 2 doi 10.1002/0471142735.im2002s39.
- Goddard E, Fischer J, Schedin P. A portal vein injection model to study liver metastasis of breast cancer. *J Vis Exp* 2016; doi: 10.3791/54903.
- Jindal S, Gao D, Bell P, Albrektsen G, Edgerton SM, Ambrosone CB, et al. Postpartum breast involution reveals regression of secretory lobules mediated by tissue-remodeling. *Breast Cancer Res* 2014;16:R31.
- Wyld L, Gutteridge E, Pinder SE, James JJ, Chan SY, Cheung KL, et al. Prognostic factors for patients with hepatic metastases from breast cancer. *Br J Cancer* 2003;89:284–90.
- Ahn SG, Lee HM, Cho SH, Lee SA, Hwang SH, Jeong J, et al. Prognostic factors for patients with bone-only metastasis in breast cancer. *Yonsei Med J* 2013;54:1168–77.
- Maller O, Hansen KC, Lyons TR, Acerbi I, Weaver VM, Prekeris R, et al. Collagen architecture in pregnancy-induced protection from breast cancer. *J Cell Sci* 2013;126(Pt 18):4108–10.
- Clasquin MF, Melamud E, Rabinowitz JD. LC-MS data processing with MAVEN: a metabolomic analysis and visualization engine. *Curr Protoc Bioinformatics* 2012;Chapter 14:Unit14 1 doi 10.1002/0471250953.bi1411s37.
- Hill RC, Calle EA, Dzieciatkowska M, Niklason LE, Hansen KC. Quantification of extracellular matrix proteins from a rat lung scaffold to provide a molecular readout for tissue engineering. *Mol Cell Proteomics* 2015;14:961–73.
- Wisniewski JR, Zougman A, Nagaraj N, Mann M. Universal sample preparation method for proteome analysis. *Nat Methods* 2009;6:359–62.
- MacLean B, Tomazela DM, Shulman N, Chambers M, Finney GL, Frewen B, et al. Skyline: an open source document editor for creating and analyzing targeted proteomics experiments. *Bioinformatics* 2010;26:966–8.

CANCER DISCOVERY

The Rodent Liver Undergoes Weaning-Induced Involution and Supports Breast Cancer Metastasis

Erica T. Goddard, Ryan C. Hill, Travis Nemkov, et al.

Cancer Discov Published OnlineFirst December 14, 2016.

Updated version Access the most recent version of this article at:
doi:[10.1158/2159-8290.CD-16-0822](https://doi.org/10.1158/2159-8290.CD-16-0822)

Supplementary Material Access the most recent supplemental material at:
<http://cancerdiscovery.aacrjournals.org/content/suppl/2016/12/14/2159-8290.CD-16-0822.DC1.html>

E-mail alerts [Sign up to receive free email-alerts](#) related to this article or journal.

Reprints and Subscriptions To order reprints of this article or to subscribe to the journal, contact the AACR Publications Department at pubs@aacr.org.

Permissions To request permission to re-use all or part of this article, contact the AACR Publications Department at permissions@aacr.org.